PAPER

Check for updates

Insights into Rh size-dependent reactivity of CO_2 methanation over Rh–Al_2O_3 catalysts†

Jinshi Dong, [ID] *[a] Hongli Yang,[a] Shengtong Li,[a] Panpan Chang [ID] [a] and Jiaqiang Yang [ID] *[b]

The hydrogenation of CO_2 to methane at atmospheric pressure is a significant chemical approach to achieve carbon neutrality and gain renewable energy. However, developing catalysts with high selectivity and high methane yield remains challenging. In this study, a series of Rh–Al_2O_3 catalysts with varying Rh particle sizes were prepared by modulating the Rh loading amounts. Rh nanoparticles (Rh NPs) were found to exhibit superior performance compared to Rh single atoms (Rh SAs) under identical reaction conditions. The sharp decrease in CH_4 selectivity at high temperature is dominantly attributed to the side reaction of dry reforming of methane instead of the limitation of reaction thermodynamics. It was found that there was the coexistence of formate and CO pathways in CO_2 methanation on Rh–Al_2O_3 catalysts regardless of Rh loadings and formate pathway is dominate for CO_2 methanation when the temperature high than 400 °C. Turnover frequency (TOF) calculations indicated that the theoretical CH_4 generation frequency of Rh NP was three times higher than that of Rh SA. Kinetic experiments and DFT calculations revealed that the dissociation and activation of H_2 is the key factor affecting the performance of Rh–Al_2O_3 catalyst. This study facilitates our understanding of Rh size-dependent chemistry for CO_2 methanation reaction.

1. Introduction

As human society and industry continue to advance, the rising concentration of CO_2 in the atmosphere exacerbates the global greenhouse effect, thereby emphasizing the urgency of eliminating CO_2 waste gas and utilizing such resources.[1–4] Carbon dioxide could be converted into high value-added chemical products, including methane (CH_4), carbon monoxide (CO), methanol (CH_3OH), and even hydrocarbons, depending on the catalysts employed and specific reaction conditions.[5–11] The hydrogenation of CO_2 to CH_4 (CO_2 methanation) not only achieves CO_2 emission reduction, but also is one of the effective ways to make full use of hydrogen obtained from renewable energy sources, which is of great significance in solving the problems of energy shortage and environmental pollution.[12–16]

The molecular CO_2 is very stable and it is a great challenge to convert it to the target product methane with high selectivity. CO_2 methanation (eqn (1)) is a strongly exothermic reaction, which means that it will be limited by thermodynamic equilibrium at high temperatures.[17,18] The reaction is accompanied

by other side reactions such as reverse water gas shift (eqn (2), RWGS) and dry reforming of methane (eqn (3), DRM).[19–21] Therefore, a highly active catalyst is essential to overcome high kinetic limitations of CO_2 methanation while promoting methanation selectivity. Compared to other supported metals, supported Rh catalysts exhibit excellent catalytic performance and methane selectivity in CO_2 methanation reactions.[22–27] Previous studies indicated that CeO_2, TiO_2, ZrO_2, and Al_2O_3 have been used as the support to investigate the catalytic performance of metal oxide-supported Rh catalysts in CO_2 hydrogenation, among which the highest CO_2 conversion towards methane is obtained for the Rh–Al_2O_3, benefiting from the strong adsorption capacity of the Al_2O_3 support for CO_2.[19,28]

$$CO_2 + 4H_2 \leftrightarrow CH_4 + 2H_2O; \Delta H_{298K} = -165 \text{ kJ mol}^{-1} \quad (1)$$

$$CO_2 + H_2 \leftrightarrow CO + H_2O; \Delta H_{298K} = 41.2 \text{ kJ mol}^{-1} \quad (2)$$

$$CO_2 + CH_4 \leftrightarrow 2CO + 2H_2; \Delta H_{298K} = 247 \text{ kJ mol}^{-1} \quad (3)$$

It is widely accepted that the CO_2 methanation reaction activity and selectivity can be tuned by controlling metal particle size, elemental doping, and metal–support interactions.[3,6,23,24,29–36] Karelovic et al.[29] reported that larger Rh particles are up to four times more active than smaller particles at low temperature (135–150 °C), whereas at higher temperatures (200 °C) the influence of Rh particle size on catalytic activity is insignificant. A similar phenomenon was found in the

[a] Laboratory of New Energy and Environmental Catalysis, School of Biological and Chemical Engineering, Guangxi University of Science and Technology, Liuzhou 545006, Guangxi, China. E-mail: jinshidong@gxust.edu.cn

[b] Zhongyuan Critical Metals Laboratory, Zhengzhou University, Zhengzhou 450001, Henan, China. E-mail: jqyang@zzu.edu.cn

Rh–TiO$_2$ catalyst system, but the catalytic properties did not change appreciably when the particle size was increased to about 7 nm.[25] Bentrup et al.[33] studied the modification of Rh–Al$_2$O$_3$ catalysts with Ni and K to vary their acidity/basicity and redox behavior and found that the Ni modification promotes the formation of CH$_4$, whereas K modification enhances the CO formation. Siang et al.[23] showed that the metal–support interaction and the degree of basicity are significantly enhanced with increasing Rh contents, which facilitates CO$_2$ adsorption and reduces the activation barriers (from 110.2 to 19.7 kJ mol^{-1}) during the methanation reaction, thereby promoting catalytic activity.

Despite so much progress up to now, the fundamental factors affecting CH$_4$ product yield still remain highly controversial. In order to gain deeper insights into the influence of particle size on catalytic activity and selectivity, a series of Al$_2$O$_3$-supported Rh catalysts with varying Rh particle sizes were synthesized and subsequently analyzed to reveal the structure–performance relationship for CO$_2$ methanation. Our findings indicate that the adsorption and activation of H$_2$ are critical factors influencing product selectivity and larger Rh particle sizes would facilitate H$_2$ activation, thereby enhancing CO$_2$ methanation activity. The decreased CH$_4$ selectivity at high temperatures is mainly due to the side reaction of dry reforming of methane. Furthermore, in situ infrared spectroscopy studies have demonstrated that both the formate and CO pathways are main reaction pathways for the CO$_2$ methanation reaction catalyzed by the Rh–Al$_2$O$_3$ catalyst.

2. Experimental section

2.1. Synthesis of Rh–Al$_2$O$_3$ catalysts

Rh–Al$_2$O$_3$ catalysts were prepared by incipient wetness impregnation (IWI) using ammonium aquopentachlororhodate ((NH$_4$)$_2$RhCl$_5$·H$_2$O, Macklin) and γ-alumina (Macklin). The quantity of (NH$_4$)$_2$RhCl$_5$·H$_2$O necessary for each weight loading was dissolved in a small beaker with 500 μL of water. Four weight loads of rhodium (0.1%, 0.5%, 1% and 2%, weight fractions) were deposited on the Al$_2$O$_3$ powder in the crucible, to produce total sample masses of 300 mg. The samples were dried under an infrared lamp, ground up with a mortar and pestle, and then calcined at 400 °C in air for 4 h in a muffle furnace to obtain catalysts with different Rh loads, which were designated as 0.1–2Rh–Al$_2$O$_3$.

2.2. Catalyst characterization

The samples were characterized using a JEM-ARM 200F transmission electron microscope (TEM) at an acceleration voltage of 200 kV. The sample powder was sonicated and suspended in ethanol solution and added drop by drop to the carbon-coated copper mesh sample rack. The particle diameter of the sample was measured by DigitalMicrograph software to determine the Rh particle size distribution. The Rh content was determined by inductively coupled plasma (ICP) spectrometry on an Agilent 5800 instrument. Prior to testing, approximately 30 mg of sample was dissolved in nitrohydrochloric acid and kept in a digester for 30 min.

CO adsorption diffuse reflectance infrared Fourier transform spectroscopy (CO-DRIFTS) was conducted on a Nicolet iS50 FTIR spectrometer equipped with a ZnSe window sample tank in a pike high temperature reaction chamber. Approximately 20 mg of catalyst was loaded into a sample tank, with the bottom surface lined with quartz wool and a metal mesh positioned beneath to prevent the obstruction of the gas outlet. The samples were pretreated by reduction in 5% H$_2$/Ar (100 mL min^{-1}) at 300 °C for 15 min before testing. After cooling to room temperature (RT), the system was purged with Ar for 10 min, and then the spectrum was recorded as the background. Subsequently, a 10% CO/Ar (50 mL min^{-1}) gas flow was introduced into the sample tank and held for 3 min and then the inlet flow was switched to Ar (100 mL min^{-1}) and held for 60 s, afterwards the spectrum was recorded.

In a typical in situ DRIFTS measurement, ~15 mg of catalyst was used, and the reduction pretreatment and background acquisition operations were the same as above. Afterwards, the reaction atmosphere was introduced. The raw gas of CO$_2$ hydrogenation consists of 1% CO$_2$ and 5% H$_2$ in a balanced mixture with 94% Ar (sourcing from 10% CO$_2$/Ar, 20% H$_2$/Ar and 99.99% Ar, Liuzhou Huaao Gas Company Limited), with a total flow rate of 40 mL min^{-1}. The sample was heated to the target temperature at a rate of 15 °C min^{-1}, held for 2 min, and then the spectra were recorded. The CO-DRIFTS measurement of the spent catalyst after the 400 °C in situ reaction was the same as the method of fresh catalyst after reduction pretreatment.

X-ray photoelectron spectroscopy (XPS) analysis was performed using a Thermo Fisher Scientific K-Alpha spectrometer equipped with a monochromatic Al Kα X-ray source (1486.6 eV) operating at 12 kV. All catalyst samples were promptly transferred to vacuum tubes within an Ar-filled glove box and maintained under specified atmospheric conditions, before XPS testing. The samples were also loaded onto the holder in the glove box to prevent oxidation of Rh states. For XPS characterization of samples before the reaction, the samples were reduced in 5% H$_2$/Ar (100 mL min^{-1}) at 300 °C for 15 min on a Beijing Builder PCA-1200 chemisorption analyzer and cooled down in the reduction atmosphere then kept in sealed centrifuge tube. The spectrum of spent catalyst after 400 °C in situ DRIFTS reaction was also recorded. After the measurements, all binding energies were charge-corrected using the dominant sp^2-hybridized carbon component (C–C/C–H) −40 of the C 1s adventitious carbon peak fixed at 284.8 eV. The fitting residual is controlled within ±0.1 eV. XPS peak fitting was performed with XPSPEAK, the baseline used a Shirley non-linear sigmoid-type. Rhodium was analyzed on the 3d$_{5/2}$ and 3d$_{3/2}$ doublet separated from 4.84 eV. The ratio of peak areas for Rh 3d$_{5/2}$ and Rh 3d$_{3/2}$ is constrained to 3 : 2. The fraction of rhodium in a metallic state was evaluated as the ratio between atomic surface concentration of Rh^0 and the total Rh concentration (Rh^0/Rh$_{tot}$).

2.3. Computational details

The density functional theory (DFT) calculations were present in supplementary Note 1 in the ESI.†

2.4.   Catalytic activity and kinetics measurements

A typical CO_2 hydrogenation activity evaluation test was performed by mixing 50 mg of catalyst with 750 mg of quartz sand uniformly filled between quartz wool in a U-shaped quartz tube reactor. The tests were carried out at a heating rate of 15 °C min^{-1}. The reaction atmosphere comprised 1% CO_2 and 5% H_2 in a balanced mixture with Ar (sourced from 10% CO_2/Ar, 20% H_2/Ar and 99.99% Ar, Liuzhou Huaao Gas Company Limited), with a total flow rate of 100 mL min^{-1}. An on-line gas chromatograph was used to quantitatively analyse the reactants and product gases. FID1 was used to detect organics in this experiment and the CH_4 converter equipped with FID2 was used to detect CO, CO_2, CH_4. Before the test, the catalysts were reduced in 5% H_2/Ar at 300 °C for 15 min with at a flow rate of 100 mL min^{-1}. CO_2 conversion and product selectivity were calculated using the following equation:

$$\text{Conversion}_{CO_2} = \frac{(n_{CO_2,\text{in}} - n_{CO_2,\text{out}})}{n_{CO_2,\text{in}}}$$

$$\text{Selectivity}_{CH_4 \text{ or } CO} = \frac{n_{CH_4 \text{ or } CO}}{(n_{CH_4} + n_{CO})}$$

Temperature programmed surface reaction (TPSR) test pretreatment conditions and experimental conditions were consistent with the activity evaluation test. The concentrations of CO_2, H_2, CO and CH_4 were monitored using the HPR-20 R&D online Mass Spectrometer (Hiden Co. Ltd). Prior to the test, the initial gas concentration was calibrated using the quantitative analysis software "QGA Professional" according to the exact flow rate of each gas measured by the mass flowmeter. The kinetic measurements of the CO_2 hydrogenation reaction were performed under the condition that CO_2 conversion was controlled at a low level (below 20%). In order to prove that our kinetic testing conditions are limited neither by mass transfer nor by heat transfer, we conducted the calculations of Weisz–Prater criteria (C_{WP}) and Mears criteria (C_M) for all catalysts with CO_2 conversions higher than 20% (uniformly applying the values at 500 °C), and the calculation results show that the mass transfer and heat transfer effects can be entirely ignored in our system. Detailed calculation processes are shown in ESI Note 2.†

3.   Results and discussion

3.1   Morphology of Rh–Al$_2$O$_3$

A series of Rh–Al_2O_3 catalysts with Rh loadings from 0.1 to 2 wt% were synthesized by the method of incipient wetness impregnation, subsequently calcined at 400 °C for 4 h, and reduced in 5% H_2/Ar at 300 °C for 15 min. Fig. 1 shows the TEM images of Rh–Al_2O_3 with different loadings after reduction. The presence of Rh single atoms (Rh SA) was detected in all catalysts despite various loading, as indicated by the red circles (Fig. 1). To prove the presence of the single-atom catalysts, we took TEM images of the Al_2O_3 support without Rh loading and confirmed that there was no white dot on its surface (Fig. S1†). We classified the nanoparticle by two criterions: (1) the amount of
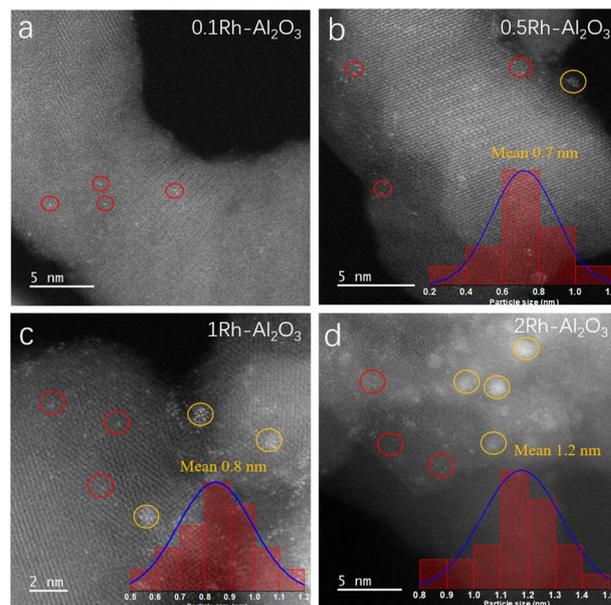

Fig. 1   TEM images of reduced (a) 0.1Rh–Al_2O_3, (b) 0.5Rh–Al_2O_3, (c) 1Rh–Al_2O_3 and (d) 2Rh–Al_2O_3 catalysts.

aggregated Rh atoms is more than 4; (2) the distance between each atom is not more than 0.4 nm. It is notable that Rh NPs are present in all samples and marked by yellow circles (Fig. 1b–d), with the exception of the sample with a Rh loading of 0.1 wt%. The results of particle size statistics show that the particle sizes of Rh increase with the increase of Rh loading. The exclusive Rh SA was further verified by the HAADF-TEM image as shown in Fig. S2.† The TEM images of before reduction are shown in Fig. S3.† It is found that the mean particle size of the catalyst after reduction increases, indicating that sintering occurs during the reduction process.

3.2   Catalytic performances of Rh–Al$_2$O$_3$ in CO$_2$ hydrogenation

Variations in the catalytic environment and reaction conditions can lead to the formation of diverse products; the primary products of CO_2 hydrogenation include methane, methanol, carbon monoxide, among others.[3,8,34,37] In this study, the products of CO_2 hydrogenation were identified as two carbon-containing substances, namely methane (CH_4) and carbon monoxide (CO), through online gas chromatography for quantitative analysis of the gas (Fig. S4†). The catalytic performance of CO_2 hydrogenation over Rh–Al_2O_3 catalysts with varying loadings was evaluated at atmospheric pressure and CO_2/H_2 = 1/5, and the findings are presented in Fig. 2. It can be seen that the catalytic activity and product selectivity changed significantly with the increasing of Rh loading. At the same reaction temperature, the CO_2 reaction rate gradually increased with the increasing in Rh loading. Nevertheless, when the Rh loading was increased from 1% to 2%, the enhancement in CO_2 reaction rate under identical conditions was not significant, indicating that the number of Rh active sites was sufficient to effectively
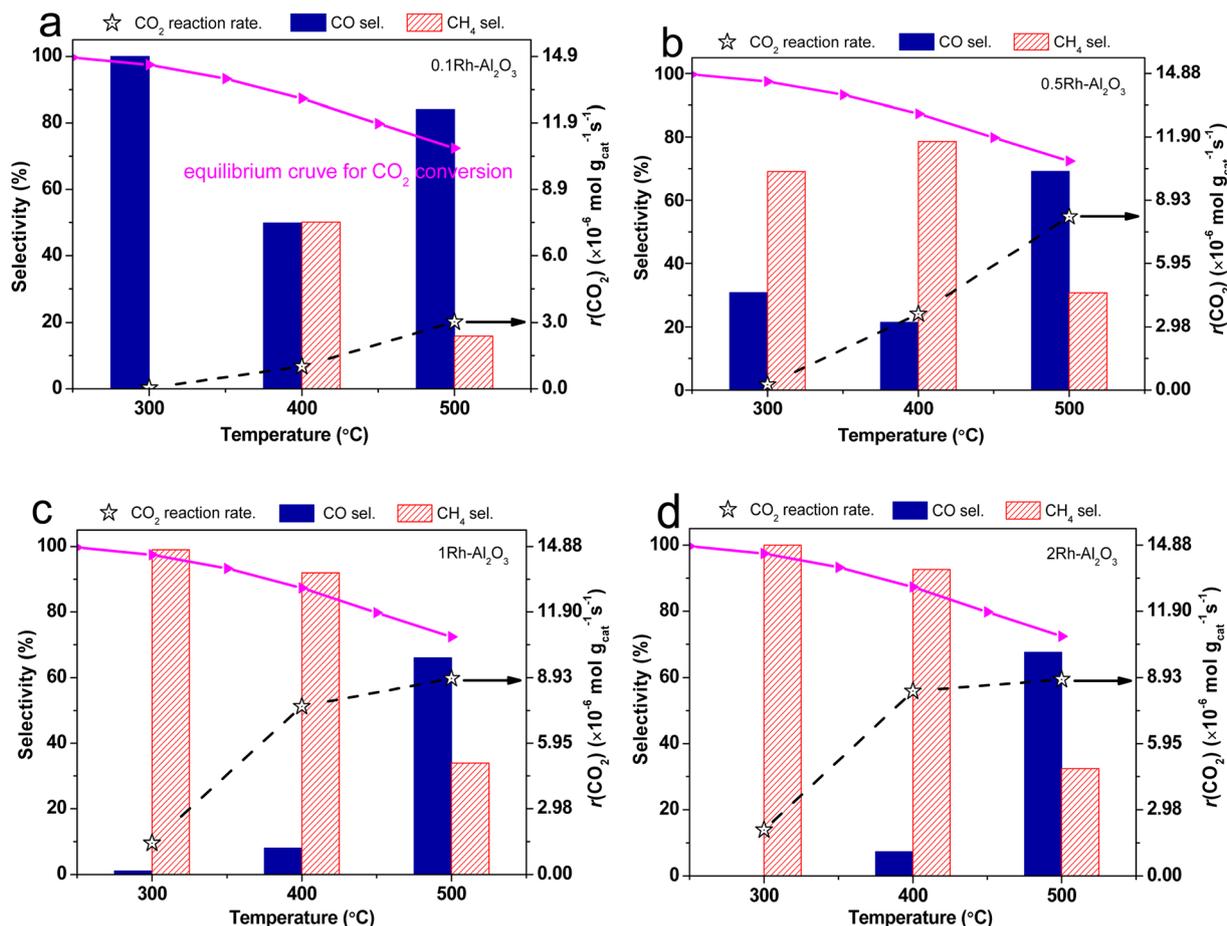
Fig. 2 The CO_2 reaction rate and product selectivity of (a) 0.1Rh–Al_2O_3, (b) 0.5Rh–Al_2O_3, (c) 1Rh–Al_2O_3 and (d) 2Rh–Al_2O_3 at different temperatures. Equilibrium conversions for CO_2 methanation (pink line) as a function of temperature are plotted. The catalyst was reduced by 5% H_2/Ar at 300 °C for 15 min before the reaction. Feed gas stream: 1% CO_2 and 5% H_2 balanced with Ar, flow rate: 100 mL min^{-1}. 50 mg catalyst was used for each sample.

convert CO_2 under the experimental conditions with a Rh loading of 1%. In all Rh–Al_2O_3 catalyst samples, the reaction rate of CO_2 exhibited a gradual increasing trend with the elevation of reaction temperature. However, the reaction rates of the 1Rh–Al_2O_3 and 2Rh–Al_2O_3 catalysts exhibited only marginal increases when the temperature was elevated from 400 °C to 500 °C. This observation indicates that the CO_2 reaction rate is constrained by the thermodynamic equilibrium of the reaction; it is difficult to continue to increase up to ~60% under the conditions of the present experiments.

It is also noteworthy that product selectivity showed a tendency towards regular change. At the same temperature, the CH_4 selectivity gradually increased and the CO selectivity decreased with the increase of Rh loading, but when Rh loading was increased from 1% to 2%, the CH_4 selectivity under the same conditions showed an insignificant increase, and the decrease in CO selectivity was also not obvious. Studies above have indicated that further increases in Rh loading do not result in a significant enhancement in CH_4 selectivity and a loading of 1% Rh could represent the optimal condition for the CO_2 methanation reaction. Furthermore, methane production was

not observed for 0.1Rh–Al_2O_3 at 300 °C, indicating that Rh NPs exhibit superior CO_2 methanation activity compared to Rh SAs at low temperatures.

In order to reveal the difference of intrinsic performance between catalysts with different Rh loadings, we used the temperature programmed surface reaction (TPSR) method to investigate the real-time concentration changes of the reactants CO_2 and H_2 and the products CH_4 and CO. The partial pressure signals of CH_4 ($m/z = 16$), CO ($m/z = 28$), CO_2 ($m/z = 44$) and H_2 ($m/z = 2$) were recorded by mass spectrometry (MS) in real time from 200 °C to 500 °C, as shown in Fig. 3. It can be observed that the reaction starting temperatures (288 °C, 240 °C, 234 °C and 206 °C, respectively) decreased with increasing of Rh loading, indicating that a higher loading of Rh favors higher reaction activity. Meanwhile, the concentration of CH_4 and CO gradually increased with the Rh loading increasing at temperatures lower than 400 °C, which is consistent with the conclusion of Fig. 2. This is because the rising reaction temperatures accelerate both CO_2 methanation and reverse water–gas shift (RWGS) reactions for CO_2 conversion. It is noteworthy that when operated temperatures exceeded approximately 415 °C, the partial
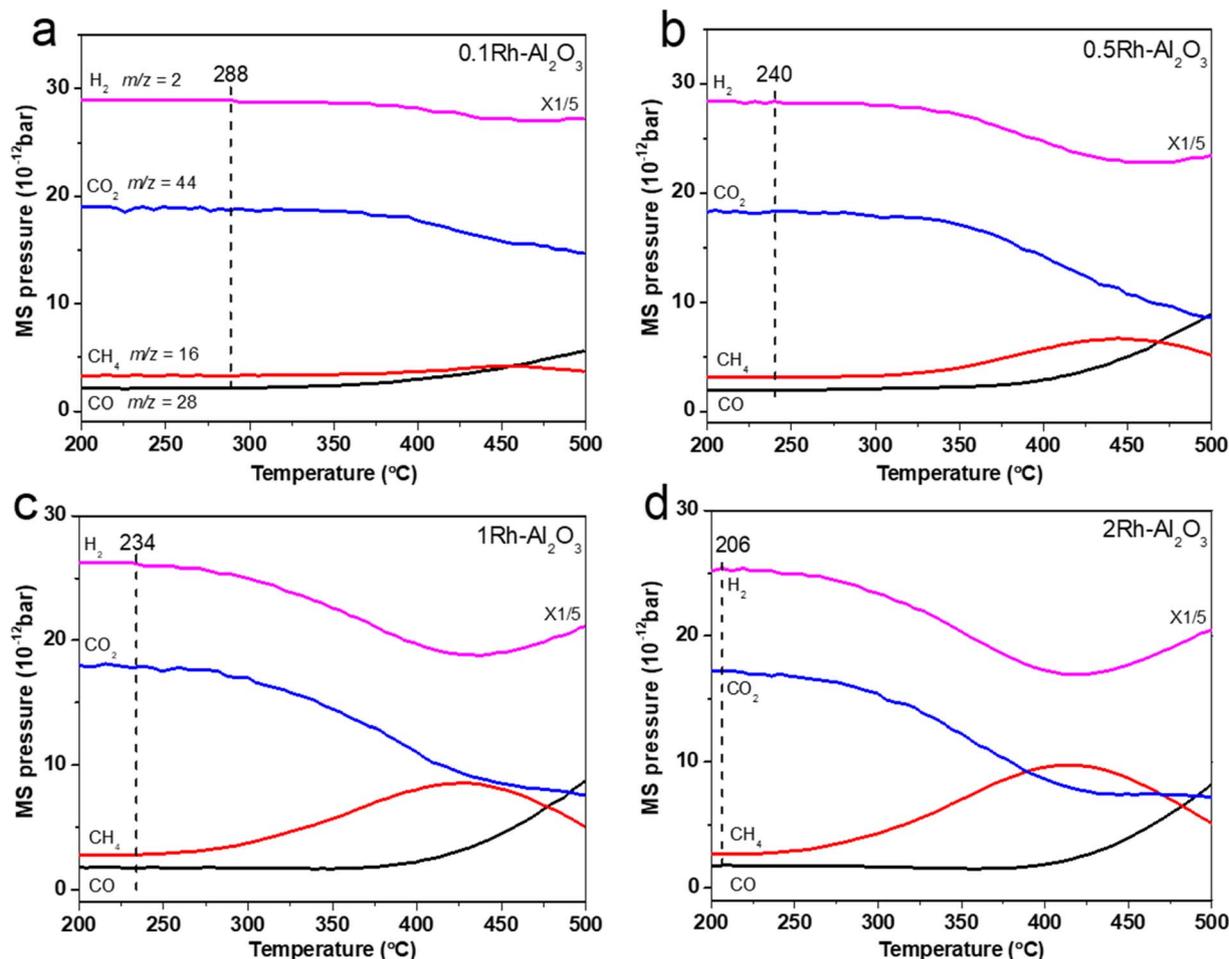
Fig. 3 The TPSR profiles of (a) 0.1Rh–Al$_2$O$_3$, (b) 0.5Rh–Al$_2$O$_3$, (c) 1Rh–Al$_2$O$_3$ and (d) 2Rh–Al$_2$O$_3$. The TPSR experimental conditions were the same as those for activity evaluation.

pressure of CO initially increased while that of CH$_4$ posed a gradual decline. Concurrently, the partial pressure of CO$_2$ fell at slower rate for 1Rh–Al$_2$O$_3$ and 2Rh–Al$_2$O$_3$ samples, whereas H$_2$ partial pressure started rising. This indicated that a side reaction occurred and resulted in hydrogen production at elevated temperatures. Combined with higher temperature conditions for hydrogen production and concentration changes of reactants, we infer that dry reforming of methane (DRM) side reactions occurred at temperatures higher than 415 °C.[38] To verify the existence of DRM reaction at high temperature, we carried out the temperature-programmed surface reaction (TPSR) of DRM on 1Rh–Al$_2$O$_3$ (Fig. S5†). The generation of H$_2$ and CO begins at ~400 °C because of the strongly endothermic characteristic ($\Delta H = +247$ kJ mol^{-1}), which is in well line with DRM reaction occurring at ~415 °C in our system. Combined with the actual CO$_2$ conversion curve in Fig. 2, it is proposed that the decrease of CH$_4$ concentration at high temperatures is mainly ascribed to the consuming of methane in dry reforming, rather than being limited by thermodynamic equilibrium.

Fig. 4a showed the CO-DRIFTS spectra of Rh–Al$_2$O$_3$ before reaction. Both peaks at ~2087 and ~2016 cm^{-1} can be observed in all the catalysts, which are attributed to the symmetric and asymmetric stretching vibrations of Rh(CO)$_2$ adsorbed on Rh SAs, respectively.[30,39] However, when the Rh loading exceeds 0.1 wt%, two distinct adsorption peaks emerge at approximately 1867 cm^{-1} and 2053 cm^{-1}, ascribed to bridge and linear CO adsorption vibrations on Rh NPs, respectively.[30,39] As the Rh loading increases, the CO adsorption signal on Rh NPs progressively intensifies, corresponding to the rise in a quantity of Rh NPs, which aligns with TEM image presented in Fig. 1. Fig. 4b showed the CO-DRIFTS spectra falling to room temperature after reaction at 400 °C. It can be seen that the various peaks appear at almost the same positions as peaks in the samples before reaction, indicating that the form of Rh remains unchanged in all the Rh–Al$_2$O$_3$ catalysts after the reaction. The redshift of the CO adsorption peak after the reaction mainly originates from the change in the electronic state of Rh ($\Delta\nu \approx 7$ cm^{-1}) such as the aggregation of Rh single atoms and instrumental errors or minor environmental fluctuations ($\Delta\nu \approx 5$ cm^{-1}), rather than from changes in the particle morphology.

Furthermore, the stability of four Rh–Al$_2$O$_3$ catalysts was studied through durability tests (Fig. S6†). The results show that the CO$_2$ conversion rate of the 0.1Rh–Al$_2$O$_3$ catalyst drops to
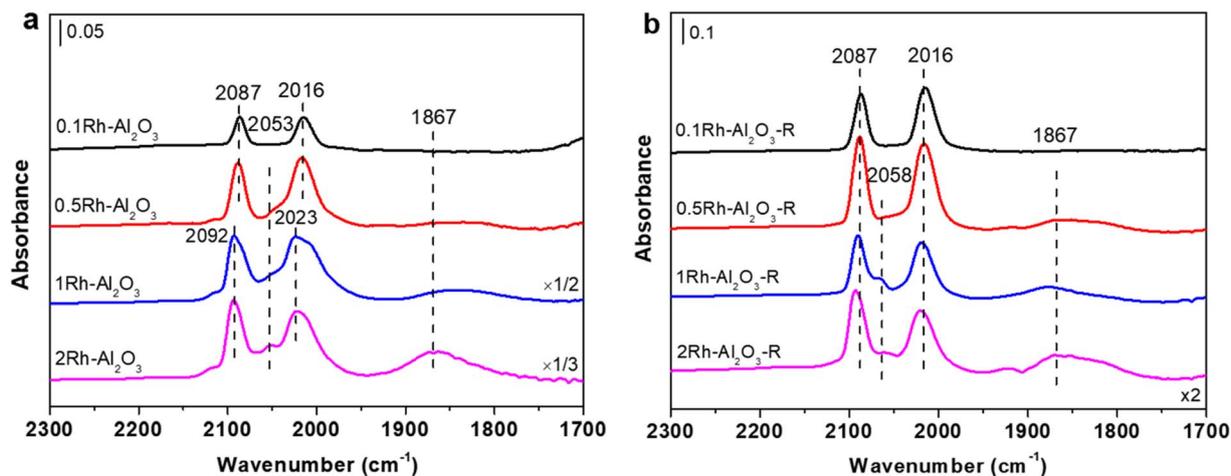
Fig. 4   Room temperature CO-DRIFT spectra of Rh–Al$_2$O$_3$ with different loadings. (a) Before reaction, (b) after reaction at 400 °C. The catalyst was treated with 5% H$_2$/Ar at 300 °C for 15 minutes before the test. CO$_2$ hydrogenation reaction conditions: 1% CO$_2$ and 5% H$_2$ balanced with Ar, flow rate: 40 mL min^{-1}. 20 mg catalyst was used for each sample.
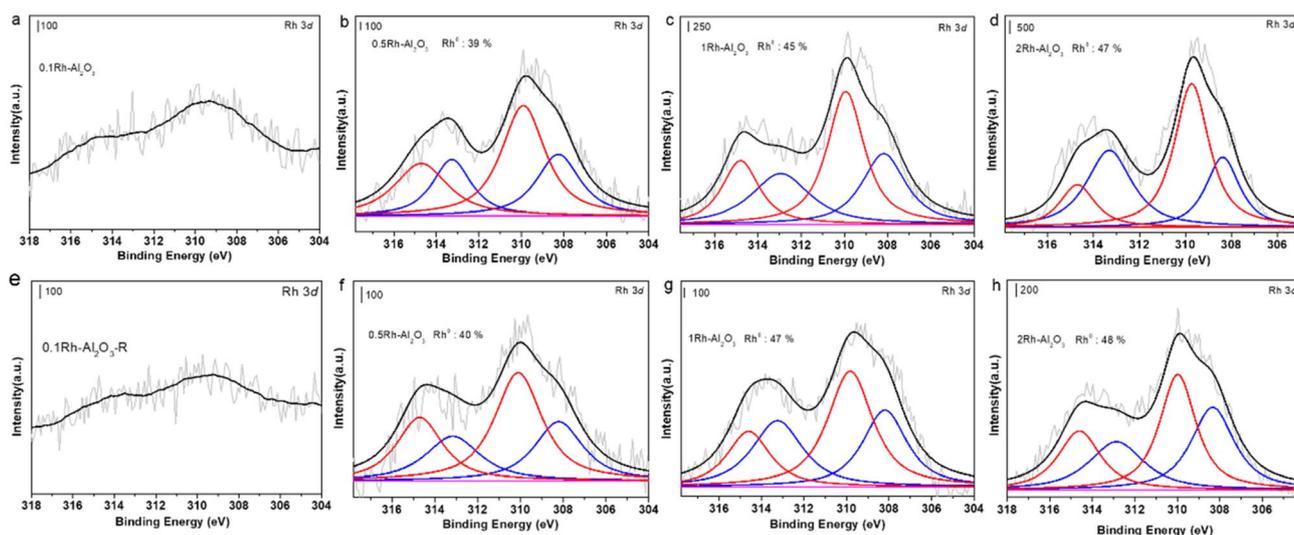

Fig. 5   XPS spectra in the Rh 3d region of different loadings Rh–Al$_2$O$_3$. (a–d) Before reaction, (e–h) after reaction at 400 °C. All catalysts before reaction were pretreated by reduction in 5% H$_2$/Ar at 300 °C for 15 min before testing.

zero within one hour of the reaction, indicating that the isolated Rh single atom is unstable under the reaction conditions and deactivates rapidly. The CO$_2$ conversion rate of the 0.5–2Rh–Al$_2$O$_3$ catalyst remained basically unchanged within 10 hours, demonstrating excellent long-term stability. The CO-DRIFTS spectra of the catalysts after the durability test showed that the 0.1Rh–Al$_2$O$_3$ catalyst exhibits bridging (1867 cm^{-1}) and linear CO (2053 cm^{-1}) adsorption vibrations on Rh NPs (Fig. S7†), which strongly indicates that isolated Rh single atoms agglomerate to form inactive aggregates under reaction conditions. This is consistent with the phenomenon reported in our previous work that single-atom catalysts are prone to sintering at high temperatures due to the weak stability of isolated metal sites.[40,41] In contrast, the CO-DRIFTS spectra of the 0.5–2Rh–Al$_2$O$_3$ catalyst showed no significant changes compared

with those before reaction, indicating that Rh nanoparticles in these samples were stable, which is in consistence with the durability test results.

The X-ray photoelectron spectra (XPS) of the Rh–Al$_2$O$_3$ catalyst before the reaction are shown in Fig. 5a–d. The negligible signal of Rh material observed on the 0.1Rh–Al$_2$O$_3$ catalyst in Fig. 5a can be attributed primarily to the low Rh content, which falls outside the detection range of XPS spectroscopy. The peaks with binding energies of ~307.9 eV and ~310.2 eV in the Rh 3d$_{5/2}$ spectrum are attributed to Rh^0 and Rh^{3+} species, respectively;[42] with the Rh loading increases from 0.5% to 2%, the percentage of Rh^0 also rises from 39% to 47%, as shown in Fig. 5b–d. It suggests a gradual increase of the particle size of Rh, which aligns with the findings from TEM analysis. Fig. 5e–h illustrates the Rh 3d XPS spectra after the 400 °C reaction, and we observe

Table 1 Calculation of turnover frequency of CO_2 and generation frequency of CH_4

Sample	Rh actual content[a] (wt%)	Rh SA content[b] (wt%)	Rh NP content (wt%)	Mean size of Rh[c] NP (nm)	Rh NP dispersion[d] (%)	Rh total dispersion[e] (%)	TOF_{CO_2}, net[f] (s^{-1})	[g]TOF_{CH_4}, net (s^{-1})	TOF_{CH_4}, net of Rh[g] NP (s^{-1})
0.1Rh–Al$_2$O$_3$	0.09	0.09	—	—	—	100	0.11	0.06	—
0.5Rh–Al$_2$O$_3$	0.46	0.17	0.29	0.7	42	64	0.13	0.10	0.16
1Rh–Al$_2$O$_3$	1.16	0.19	0.97	0.8	36	46	0.15	0.14	0.18
2Rh–Al$_2$O$_3$	1.81	0.22	1.59	1.2	25	34	0.14	0.13	0.17

[a] Measured by ICP-AES. [b] Determined by the IR intensity of CO adsorption on Rh single atom (SA), and the detailed calculation is shown in Table S3. [c] Determined by TEM image counts. [d] Rh NP dispersion = 1/mean size of Rh NP × 0.3. [e] Total dispersion = (Rh SA content × 100 + Rh NP content × Rh NP dispersion)/Rh actual content. [f] Net reaction rate of CO_2, measured at 400 °C, and the detailed calculation is shown in Table S4. [g] Net CH_4 formation rate, measured at 400 °C, and the detailed calculation is shown in Table S5.

that the percentages of Rh⁰ in each catalyst after reaction have no obvious change compared to the corresponding catalysts before reaction, which is consistent with the findings in Fig. 4. The detailed results of XPS deconvolution of the Rh–Al$_2$O$_3$ catalyst are shown in Tables S1 and S2.†

The actual Rh loadings were further measured by ICP and are shown in Table 1, and it is seen that the values consequently approached the nominal Rh loading. The significant discrepancies in the stoichiometric ratios of CO adsorbed onto the surfaces of Rh SA and Rh NP, along with the variations in the ratios of CO adsorbed onto Rh NP surfaces with differing particle sizes,[33] render traditional CO chemisorption techniques inadequate for precisely determining the dispersion of Rh–Al$_2$O$_3$ samples. In this study, the Rh SA content in other Rh–Al$_2$O$_3$ samples is semi-quantified based on the adsorption strength of Rh SA in the CO-DRIFT spectrum of each Rh–Al$_2$O$_3$ sample, with the 0.1Rh–Al$_2$O$_3$ sample serving as a reference point, and corresponding calculation process is outlined in Table S3 and Fig. S8.† The dispersion of Rh NP is derived from the mean particle size of Rh NP measured by TEM particle size statistics. Fig. 1 and S9† show representative TEM images of Rh NP, and the statistical mean size of Rh NP is listed in Table 1. The Rh NP dispersion was determined by calculating the reciprocal of the average size of Rh NP (in nm) and subsequently multiplying this value by a correction factor, following the methodology outlined by Zhang et al..[43] Fig. S10† shows that the calculated Rh NP dispersion is consistent with the actual Rh NP dispersion when the correction coefficient is 0.3. Accordingly, the turnover frequency of CO_2 conversion (TOF_{CO_2}) and CH_4 generation (TOF_{CH_4}) as well as the theoretical turnover frequency of Rh NP CH_4 generation (TOF_{CH_4} of Rh NP) were calculated for the Rh–Al$_2$O$_3$ catalysts at 400 °C and detailed calculations are shown in Tables S4 and S5† As observed in Table 1, the minimal variation observed in the turnover frequency of CO_2 (TOF_{CO_2}) across different Rh–Al$_2$O$_3$ samples indicates a comparable CO_2 conversion efficiency between Rh single atoms (Rh SA) and Rh nanoparticles (Rh NP). Furthermore, the turnover frequency of CH_4 (TOF_{CH_4}) for samples containing Rh loadings exceeding 0.5% is notably higher than that of samples with a Rh loading of 0.1%. This suggests that Rh NPs exhibit a superior capacity for CH_4 generation compared to Rh SA. Additionally, the theoretical TOF_{CH_4} of Rh NP was calculated and approximately three times the value of Rh SA (Table 1), suggesting better CO_2 methanation activity of Rh sites on Rh NP than Rh SA. In this study, we conducted a comparative analysis of the turnover frequency values of CH_4 generation (TOF_{CH_4}) calculated in this work with those in CO_2 methanation using various Rh-based catalysts (Table S6†). The TOF values reported here are superior than others.

We performed kinetic experiments on the CO_2 methanation reaction on Rh–Al$_2$O$_3$, as shown in Fig. 6. From Fig. 6a, the apparent activation energy (E_a) gradually decreased with increasing Rh loading, indicating that Rh NP is more prone to catalyze CO_2 methanation reaction. In Fig. 6b, the negative measured CO_2 apparent reaction orders (n_{CO_2}) indicated that increasing partial pressure of CO_2 for 0.1% Rh-loaded catalyst would inhibit the CH_4 formation and conversely, partial
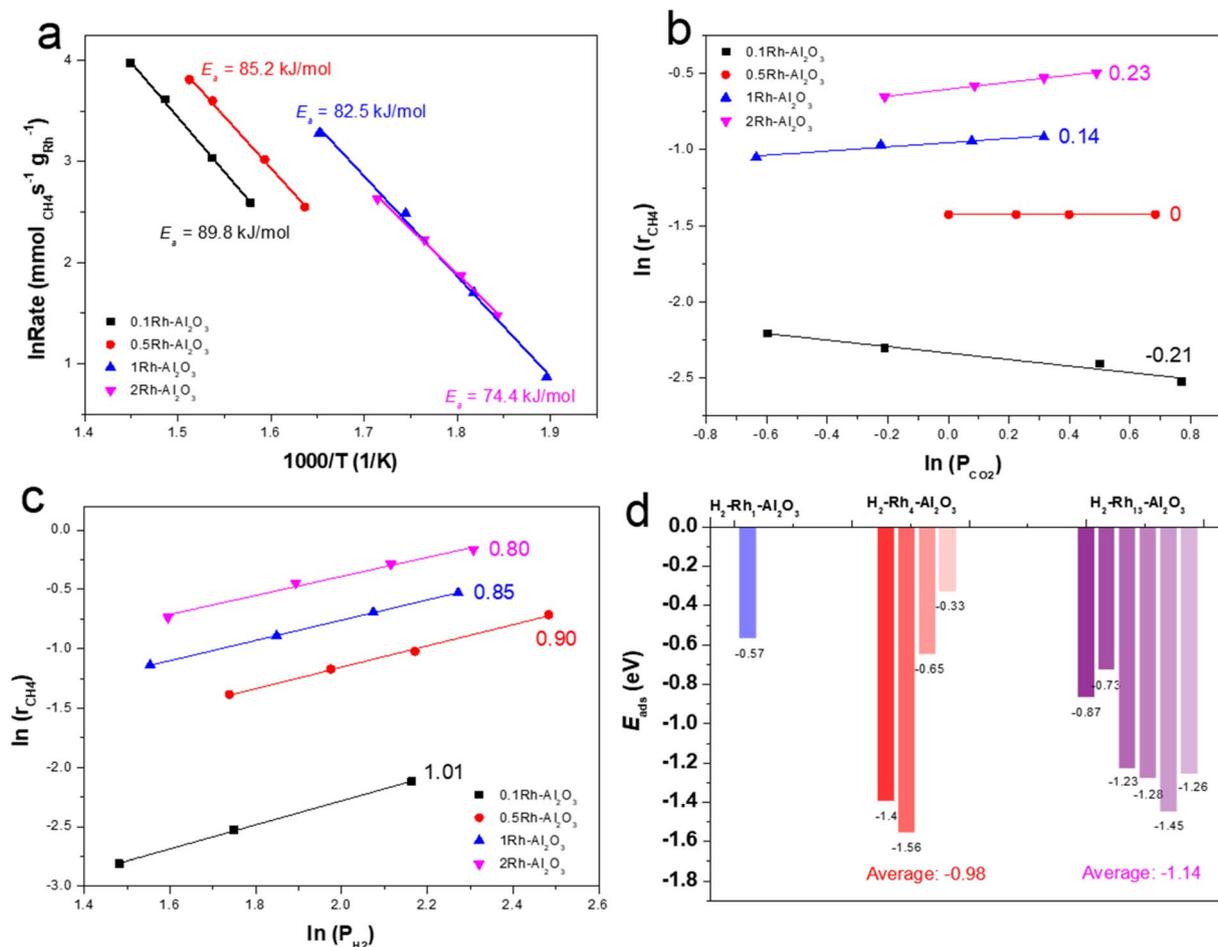
Fig. 6 Arrhenius plots of (a) CO_2 methanation reaction. Reaction orders of (b) CO_2 and (c) H_2 with the different loadings Rh–Al_2O_3 catalysts in the CO_2 methanation reactions. (d) The adsorption energies of H_2 adsorbing on Rh_1–Al_2O_3, Rh_4–Al_2O_3 and Rh_{13}–Al_2O_3 by DFT calculations.

pressure of CO_2 could achieve the different degree of enhancement in the formation rate of CH_4 for other samples, due to non-negative apparent reaction orders. In addition, the reaction orders of CO_2 (n_{CO_2}) are approximately zero (−0.21–0.23), also indicating that CO_2 adsorption and activation is not a significant influencing factor in the CO_2 methanation reaction.

On the other hand, as shown in Fig. 6c, an increase in the partial pressure of H_2 could significantly increase CH_4 formation rates for all Rh–Al_2O_3 catalyst samples, because the H_2 reaction orders (n_{H_2}) are greater than 0.80 and much higher than n_{CO_2} (Fig. 6c), suggesting that H_2 dissociation and activation should be key factors affecting catalytic performance of Rh–Al_2O_3 catalysts. In addition, the n_{H_2} gradually decreases with increasing sizes of Rh particles and it also indicates that H_2 adsorption becomes more pronounced for Rh nanoparticles with larger size, thus contributing to deep hydrogenation for the product CO or other intermediates, thereby indicating that high Rh loading favors methane generation. Subsequent density functional theory (DFT) calculations were employed to ascertain H_2 adsorption strength on different supported Rh sites. The structural models of Rh_1–Al_2O_3, Rh_4–Al_2O_3, and Rh_{13}–Al_2O_3

were used to represent Rh single atoms, Rh clusters, and Rh nanoparticles loaded on the Al_2O_3 surface, respectively[40] and the calculated results and H_2 adsorption structures are shown in Fig. 6d and Tables S7–9,† respectively. It can be found that the H_2 adsorption becomes stronger for supported Rh catalysts with larger size, which is consistent with the experimental results of the reaction orders. The reaction orders of the reverse water–gas shift (RWGS) process are not determined because of low CO_2 conversion rates of Rh–Al_2O_3 samples, with the exception of the 0.1Rh–Al_2O_3 samples (in Table S10†).

Table 2 shows the calculation results of mass and heat transfer criteria for CO_2 hydrogenation reaction with different catalysts at 773.15 K. The average particle size of catalyst was measured by laser particle size analyzer (Fig. S11†). The relevant parameters to calculate mass and heat transfer limits of CO_2 hydrogenation reaction was given in Tables S11 and S12.† The results show that both the mass transfer and heat transfer effects can be ignored under our experimental conditions.

3.3 Reaction mechanism of Rh–Al_2O_3 in CO_2 hydrogenation

In order to deeply investigate the reaction mechanism and intermediates of Rh–Al_2O_3 catalyzed CO_2 hydrogenation, the *in*

Table 2 Summary of mass and heat transfer limitations at different samples for CO_2 hydrogenation

Sample	T (K)	D_{eff} ($\times 10^{-6}$ m^2 s^{-1})	k_c (m s^{-1})	h (W m^{-2} K^{-1})	C_{WP} ($\times 10^{-3}$)	$C_{M, mass}$ ($\times 10^{-3}$)	$C_{M, heat}$ ($\times 10^{-6}$)
0.1Rh–Al$_2$O$_3$	773.15	8.09	1.15	580.04	1.32	0.132	3.73
0.5Rh–Al$_2$O$_3$	773.15	8.09	0.86	436.54	6.12	0.612	289
1Rh–Al$_2$O$_3$	773.15	8.09	0.84	426.82	7.19	0.719	400
2Rh–Al$_2$O$_3$	773.15	8.09	1.27	644.35	3.15	0.315	145

situ DRIFTS spectra of Rh–Al$_2$O$_3$ with different loadings were measured and the results are presented in Fig. 7. The peaks at 1438–1433 cm^{-1}, 1587 cm^{-1} and 1372 cm^{-1} are attributed to the absorption peaks of, CO_3^{2-}*,[32,34] the vibrations of monodentate formate (m-HCOO*) and bidentate formate (b-HCOO*), respectively.[44–46] It can be observed that the intensity of CO_3^{2-}* absorption peak decreased with increasing temperature due to CO_3^{2-}* binding with H* to produce formates, which further caused the appearance of formate signals (1587 cm^{-1} and

1372 cm^{-1})[44] and the appearance temperatures gradually decreased with the increasing Rh loading. The CO_3^{2-}* adsorption signal finally disappeared at 400 °C, 300 °C, 250 °C and 200 °C for 0.1Rh–Al$_2$O$_3$, 0.5Rh–Al$_2$O$_3$, 1Rh–Al$_2$O$_3$, 2Rh–Al$_2$O$_3$, respectively. The temperature at which HCOO* species began to decrease gradually (from 300 °C to 100 °C) with the increase of Rh loading amount. The gaseous CH$_4$ (2907 cm^{-1}) is also generated along with the HCOO* species,[33,47] suggesting that formate should be the key intermediate species for methane
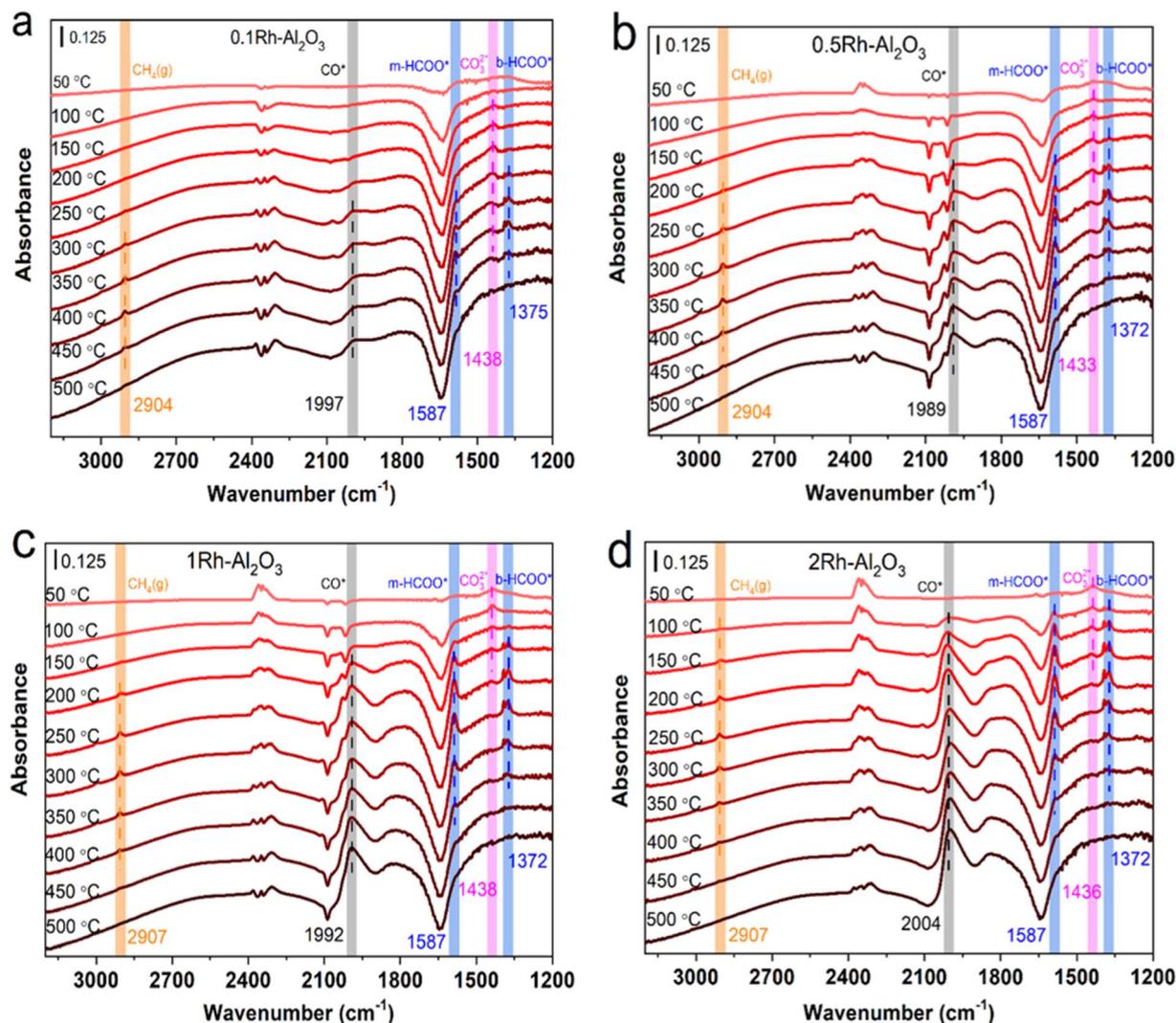

Fig. 7 *In situ* DRIFTS spectra of (a) 0.1Rh–Al$_2$O$_3$, (b) 0.5Rh–Al$_2$O$_3$, (c) 1Rh–Al$_2$O$_3$ and (d) 2Rh–Al$_2$O$_3$ during CO$_2$ hydrogenation at different temperatures.

production.[45,48,49] These results illustrated that high Rh loading would bring about the superior catalytic performance of CO_2 hydrogenation, in accordance to the catalytic performance tests in Fig. 2.

The peak appearing at ~2000 cm^{-1} is attributed to the CO adsorption peak on Rh,[20,34,50] and its appearance temperatures gradually fell with increasing Rh loadings, but the product temperature of CO gas increased with increasing Rh loadings, as shown in Fig. 3. The inconsistency suggested that the formed CO species should first be adsorbed on the surface sites and then released as gas CO *via* overcoming desorption barriers and the catalysts with higher Rh loading should pose the higher CO desorption barriers. Otherwise, it is found that the signal of CO (CO*) and gaseous CH_4 appears at the same temperature and thus it is inferred that CO* is also a crucial intermediate species of methane generation.[31,34,45,51] It is worth noting that at temperatures higher than 450 °C, the signals of gaseous CH_4 and HCOO* disappeared, but the CO adsorption signal still existed, which further confirmed that DRM or RWGS reactions occur at high temperatures. The situation agrees with the

conclusion that CO selectivity at high temperatures is enhanced as shown in Fig. 2.

To determine the change of each pathway to the formation of CH_4, the intensity of the CO* (~2000 cm^{-1}) and m-HCOO* (1587 cm^{-1}) bands were calculated by the adsorbing intensity of the highest point of the peak position minus the adsorbing intensity of the baseline in each IR spectrum. Intensity values were plotted in function of temperature for each sample, as shown in Fig. 8. It can be found that the intensities of both intermediates increase with the elevated temperatures until up to 250 °C or 300 °C for all samples. When the temperature exceeded that temperature, the intensity of HCOO* reversed to gradually decrease, illustrating the conversion of formate to the product CH_4. However, the intensity of CO* started to increase again when the temperature high than 350 °C, attributing to the produced CO species of DRM reaction at high temperature. Accordingly, both pathways contributed to CO_2 methanation reaction, the intensity of CO* increased at high temperature mainly attributed to DRM reaction, as evidenced by the TPSR results of mere DRM reaction (Fig. S5†).
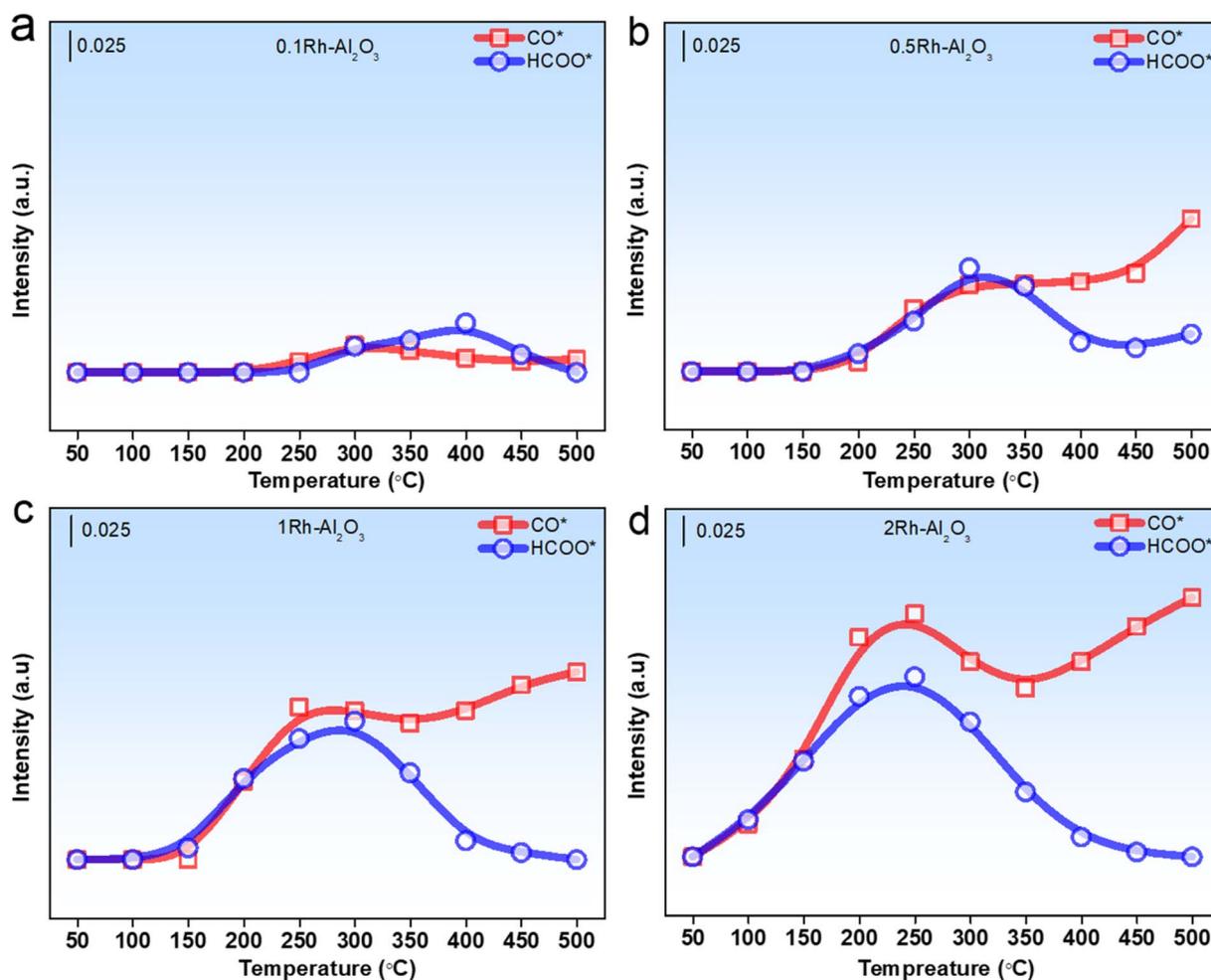

Fig. 8 *In situ* DRIFTS normalized band intensity *versus* temperature of CO* (~2000 cm^{-1}) and *m*-HCOO* (1587 cm^{-1}). (a) 0.1Rh–Al_2O_3. (b) 0.5Rh–Al_2O_3. (c) 1Rh–Al_2O_3. (d) 2Rh–Al_2O_3.

4. Conclusions

In this study, a series of Rh–Al$_2$O$_3$ catalysts with varying Rh particle sizes were prepared by modulating Rh loading amounts. TEM and CO-DRIFTS showed that the 0.1Rh–Al$_2$O$_3$ sample existed in the form of single atoms and 0.5–2Rh–Al$_2$O$_3$ catalyst samples existed with a mixture of Rh single atoms and Rh nanoparticles. The activity tests showed that the CH$_4$ selectivity gradually increased with increasing Rh loading at the same reaction temperature. The CH$_4$ yield of each Rh–Al$_2$O$_3$ catalyst first increases and then decreases with increasing reaction temperature; CH$_4$ selectivity decreases sharply at temperatures higher than 400 °C. The TPSR experiments revealed that when the temperature exceeds approximately 415 °C, the partial pressure of H$_2$ begins to increase significantly reversing from its downward trend, attributed to the occurrence of DRM reaction at elevated temperatures. Therefore, the decreased CH$_4$ selectivity at high temperatures is not entirely limited by the thermodynamics of CO$_2$ methanation, but largely due to DRM side reaction consuming large amounts of methane.

Experimental results from in *situ* infrared spectroscopy confirm that both formate and CO pathways coexist for Rh–Al$_2$O$_3$ catalyzing CO$_2$ methanation regardless of Rh loading amounts and formate pathway is dominate for CO$_2$ methanation when the temperature high than 400 °C. TOF calculation showed that TOF$_{CO_2}$ did not differ much between different Rh particle sizes, but TOF$_{CH_4}$ on Rh NP was three times higher than that of TOF$_{CH_4}$ on Rh SA, suggesting better CO$_2$ methanation activity of Rh sites on Rh NP. Overall, the reaction orders of CO$_2$ on Rh–Al$_2$O$_3$ catalyst are approximately 0, whereas n_{H_2} approaches 1 and decreases with increasing Rh loading, suggesting that H$_2$ dissociation and activation are critical factors influencing performance of Rh–Al$_2$O$_3$ catalysts. Additionally, H$_2$ adsorbed more strongly on Rh catalysts with large particle size by DFT calculations. These results substantially enhance the systematic and thorough comprehension of the catalytic hydrogenation of CO$_2$ over Rh–Al$_2$O$_3$ catalysts.

Data availability

Data will be made available on request.

Conflicts of interest

There are no conflicts to declare.

Acknowledgements

References

1 A. D. N. Kamkeng, M. Wang, J. Hu, W. Du and F. Qian, *Chem. Eng. J.*, 2021, **409**, 128138.

2 H. Sun, C. Wu, B. Shen, X. Zhang, Y. Zhang and J. Huang, *Mater. Today Sustain.*, 2018, **1–2**, 1–27.

3 H. Zheng, W. Liao, J. Ding, F. Xu, A. Jia, W. Huang and Z. Zhang, *ACS Catal.*, 2022, **12**, 15451–15462.

4 K. Li, X. Li, L. Li, X. Chang, S. Wu, C. Yang, X. Song, Z.-J. Zhao and J. Gong, *JACS Au*, 2023, **3**, 508–515.

5 S. Sharma, Z. Hu, P. Zhang, E. W. McFarland and H. Metiu, *J. Catal.*, 2011, **278**, 297–309.

6 S. Li, Y. Xu, Y. Chen, W. Li, L. Lin, M. Li, Y. Deng, X. Wang, B. Ge, C. Yang, S. Yao, J. Xie, Y. Li, X. Liu and D. Ma, *Angew. Chem., Int. Ed.*, 2017, **56**, 10761–10765.

7 O. Martin, A. J. Martín, C. Mondelli, S. Mitchell, T. F. Segawa, R. Hauert, C. Drouilly, D. Curulla-Ferré and J. Pérez-Ramírez, *Angew. Chem., Int. Ed.*, 2016, **55**, 6261–6265.

8 N. Rui, X. Wang, K. Deng, J. Moncada, R. Rosales, F. Zhang, W. Xu, I. Waluyo, A. Hunt, E. Stavitski, S. D. Senanayake, P. Liu and J. A. Rodriguez, *ACS Catal.*, 2023, **13**, 3187–3200.

9 J. Lu, B. Fu, M. C. Kung, G. Xiao, J. W. Elam, H. H. Kung and P. C. Stair, *Science*, 2012, **335**, 1205–1208.

10 K. Nakagawa, C. Kajita, K. Okumura, N.-o. Ikenaga, M. Nishitani-Gamo, T. Ando, T. Kobayashi and T. Suzuki, *J. Catal.*, 2001, **203**, 87–93.

11 X. Li, J. Lin, L. Li, Y. Huang, X. Pan, S. E. Collins, Y. Ren, Y. Su, L. Kang, X. Liu, Y. Zhou, H. Wang, A. Wang, B. Qiao, X. Wang and T. Zhang, *Angew. Chem., Int. Ed.*, 2020, **59**, 19983–19989.

12 W. Zhen, F. Gao, B. Tian, P. Ding, Y. Deng, Z. Li, H. Gao and G. Lu, *J. Catal.*, 2017, **348**, 200–211.

13 Z.-W. Zhao, X. Zhou, Y.-N. Liu, C.-C. Shen, C.-Z. Yuan, Y.-F. Jiang, S.-J. Zhao, L.-B. Ma, T.-Y. Cheang and A.-W. Xu, *Catal. Sci. Technol.*, 2018, **8**, 3160–3165.

14 F. Hu, R. Ye, C. Jin, D. Liu, X. Chen, C. Li, K. H. Lim, G. Song, T. Wang, G. Feng, R. Zhang and S. Kawi, *Appl. Catal., B*, 2022, **317**, 121715.

15 Q. Li, Y. Gao, M. Zhang, H. Gao, J. Chen and H. Jia, *Appl. Catal., B*, 2022, **303**, 120905.

16 J. Dong, D. Li, Y. Zhang, P. Chang and Q. Jin, *J. Catal.*, 2022, **407**, 174–185.

17 Y. Du, C. Qin, Y. Xu, D. Xu, J. Bai, G. Ma and M. Ding, *Chem. Eng. J.*, 2021, **418**, 129402.

18 C. Italiano, G. Drago Ferrante, L. Pino, M. Laganà, M. Ferraro, V. Antonucci and A. Vita, *Chem. Eng. J.*, 2022, **434**, 134685.

19 N. M. Martin, P. Velin, M. Skoglundh, M. Bauer and P.-A. Carlsson, *Catal. Sci. Technol.*, 2017, **7**, 1086–1094.

20 J. Ashok, S. Pati, P. Hongmanorom, Z. Tianxi, C. Junmei and S. Kawi, *Catal. Today*, 2020, **356**, 471–489.

21 C. He, Q. Li, Z. Ye, L. Wang, Y. Gong, S. Li, J. Wu, Z. Lu, S. Wu and J. Zhang, *Angew. Chem., Int. Ed.*, 2024, e202412308.

22 J.-N. Park and E. W. McFarland, *J. Catal.*, 2009, **266**, 92–97.

23 T. J. Siang, A. A. Jalil, N. A. A. Fatah and M. E. Chung, *J. Environ. Chem. Eng.*, 2021, **9**, 104616.

24 J. C. Matsubu, S. Zhang, L. DeRita, N. S. Marinkovic, J. G. Chen, G. W. Graham, X. Pan and P. Christopher, *Nat. Chem.*, 2016, **9**, 120–127.

25 A. Karelovic and P. Ruiz, *J. Catal.*, 2013, **301**, 141–153.

26 H. Arandiyan, Y. Wang, J. Scott, S. Mesgari, H. Dai and R. Amal, *ACS Appl. Mater. Interfaces*, 2018, **10**, 16352–16357.

27 R. Thalinger, T. Götsch, C. Zhuo, W. Hetaba, W. Wallisch, M. Stöger-Pollach, D. Schmidmair, B. Klötzer and S. Penner, *ChemCatChem*, 2016, **8**, 2057–2067.

28 D. Pandey and G. Deo, *J. Ind. Eng. Chem.*, 2016, **33**, 99–107.

29 A. Karelovic and P. Ruiz, *Appl. Catal., B*, 2012, **113–114**, 237–249.

30 J. C. Matsubu, V. N. Yang and P. Christopher, *J. Am. Chem. Soc.*, 2015, **137**, 3076–3084.

31 B. Yang, Y. Wang, B. Gao, L. Zhang and L. Guo, *ACS Catal.*, 2023, **13**, 10364–10374.

32 Y. Guo, S. Mei, K. Yuan, D.-J. Wang, H.-C. Liu, C.-H. Yan and Y.-W. Zhang, *ACS Catal.*, 2018, **8**, 6203–6215.

33 D. Heyl, U. Rodemerck and U. Bentrup, *ACS Catal.*, 2016, **6**, 6275–6284.

34 S. Li, Y. Xu, H. Wang, B. Teng, Q. Liu, Q. Li, L. Xu, X. Liu and J. Lu, *Angew. Chem., Int. Ed.*, 2023, **62**, e202218167.

35 X. Xu, L. Liu, Y. Tong, X. Fang, J. Xu, D.-e. Jiang and X. Wang, *ACS Catal.*, 2021, **11**, 5762–5775.

36 H. Xin, L. Lin, R. Li, D. Li, T. Song, R. Mu, Q. Fu and X. Bao, *J. Am. Chem. Soc.*, 2022, **144**, 4874–4882.

37 H. Zhao, R. Yu, S. Ma, K. Xu, Y. Chen, K. Jiang, Y. Fang, C. Zhu, X. Liu, Y. Tang, L. Wu, Y. Wu, Q. Jiang, P. He, Z. Liu and L. Tan, *Nature Catalysis*, 2022, **5**, 818–831.

38 Y. Wang, L. Li, G. Li, Q. Zhao, X. s. Wu, Y. Wang, Y. Sun and C. Hu, *ACS Catal.*, 2023, **13**, 6486–6496.

39 Y. Kwon, T. Y. Kim, G. Kwon, J. Yi and H. Lee, *J. Am. Chem. Soc.*, 2017, **139**, 17694–17699.

40 J. Dong, Y. Zhang, D. Li, A. Adogwa, S. Huang, M. Yang, J. Yang and Q. Jin, *Appl. Catal., B*, 2023, **330**, 122662.

41 J. Dong, S. Huang, S. Li, P. Chang and J. Yang, *Catal. Sci. Technol.*, 2024, **14**, 5211–5217.

42 Y. Feng, Y. Zhang, J. Wang, L. Ling, R. Zhang, M. Fan, B. Hou, D. Li and B. Wang, *ACS Catal.*, 2024, **14**, 1874–1881.

43 B. Qiao, A. Wang, X. Yang, L. F. Allard, Z. Jiang, Y. Cui, J. Liu, J. Li and T. Zhang, *Nat. Chem.*, 2011, **3**, 634–641.

44 A. Cárdenas-Arenas, A. Quindimil, A. Davó-Quiñonero, E. Bailón-García, D. Lozano-Castelló, U. De-La-Torre, B. Pereda-Ayo, J. A. González-Marcos, J. R. González-Velasco and A. Bueno-López, *Appl. Catal., B*, 2020, **265**, 118538.

45 C. Wang, Y. Lu, Y. Zhang, H. Fu, S. Sun, F. Li, Z. Duan, Z. Liu, C. Wu, Y. Wang, H. Sun and Z. Yan, *Nano Res.*, 2023, **16**, 12153–12164.

46 A. Holmgren, B. Andersson and D. Duprez, *Appl. Catal., B*, 1999, **22**, 215–230.

47 R.-P. Ye, Q. Li, W. Gong, T. Wang, J. J. Razink, L. Lin, Y.-Y. Qin, Z. Zhou, H. Adidharma, J. Tang, A. G. Russell, M. Fan and Y.-G. Yao, *Appl. Catal., B*, 2020, **268**, 118474.

48 F. Wang, S. He, H. Chen, B. Wang, L. Zheng, M. Wei, D. G. Evans and X. Duan, *J. Am. Chem. Soc.*, 2016, **138**, 6298–6305.

49 B. Miao, S. S. K. Ma, X. Wang, H. Su and S. H. Chan, *Catal. Sci. Technol.*, 2016, **6**, 4048–4058.

50 Y. Tang, T. Zhao, H. Han, Z. Yang, J. Liu, X. Wen and F. Wang, *Adv. Sci.*, 2023, **10**, 2300122.

51 Y. Li, Z. Liu, Z. Rao, F. Yu, W. Bao, Y. Tang, H. Zhao, J. Zhang, Z. Wang, J. Li, Z. Huang, Y. Zhou, Y. Li and B. Dai, *Appl. Catal., B*, 2022, **319**, 121903.